Bone 127 (2019) 526–536

Contents lists available at ScienceDirect

Bone

journal homepage: www.elsevier.com/locate/bone

Full Length Article

3D analysis of the osteonal and interstitial tissue in human radii cortical bone

Rémy Gauthier[a,b], Hélène Follet[c], Cécile Olivier[b], David Mitton[a], Françoise Peyrin[b,*]

[a] Univ Lyon, Université Claude Bernard Lyon 1, IFSTTAR, LBMC UMR_T9406, F69622 Lyon, France
[b] Univ Lyon, CNRS UMR 5220, Inserm U1206, INSA Lyon, Université Claude Bernard Lyon 1, Creatis, F69621 Villeurbanne Cedex, France
[c] Univ Lyon, Université Claude Bernard Lyon 1, INSERM, LYOS UMR1033, F69008 Lyon, France

ARTICLE INFO

Keywords:
Human cortical bone
Synchrotron radiation
Micro-computed tomography
Osteons
Cement lines
Osteocytes lacunae

ABSTRACT

Human cortical bone has a complex hierarchical structure that is periodically remodelled throughout a lifetime. This microstructure dictates the mechanical response of the tissue under a critical load. If only some structural features, such as the different porosities observed in bone, are primarily studied, then investigations may not fully consider the osteonal systems in three-dimensions (3D). Currently, it is difficult to differentiate osteons from interstitial tissue using standard 3D characterization methods. Synchrotron radiation micro-computed tomography (SR-μCT) in the phase contrast mode is a promising method for the investigation of osteons. In the current study, SR-μCT imaging was performed on cortical bone samples harvested from eight human radii (female, 50–91 y.o.). The images were segmented to identify Haversian canals, osteocyte lacunae, micro-cracks, as well as osteons. The significant correlation between osteonal and Haversian canal volume fraction highlights the role of the canals as sites where bone remodelling is initiated. The results showed that osteocyte lacunae morphometric parameters depend on their distance to cement lines, strongly suggesting the evolution of biological activity from the beginning to the end of the remodelling process. Thus, the current study provides new data on 3D osteonal morphometric parameters and their relationships with other structural features in humans.

1. Introduction

Bone fragility generated by diseases such as osteoporosis is known to be associated with structural changes in the tissue [1].

The difficulty in predicting such increases in fragility is mainly due to the highly complex organization of the tissue. Bone structure is made up of different features observed at different length scales, from the collagen fibril up to the osteonal system, which includes osteocyte lacunae and vascular canals [1–4]. All of these length scales are assumed to be involved in cortical bone crack propagation mechanisms such as micro-cracking or crack deflection [5–10]. However, despite several qualitative observations regarding the implication of osteons in the crack deflection mechanism [11,12], only a few studies provide quantitative 3D data due to the difficulty in quantifying their morphometric properties [9,13,14].

Osteonal areas arise in cortical bone through a remodelling process at the surface of osteonal canals [15–18], and as such, they surround these canals. The remodelling process consists of the formation of young tissue to replace older, damaged tissue through cellular mechanisms [19,20]. As mineralization increases with time [21–23], new remodelled tissue is less mineralized than older tissue. As such, the osteon is different from its surrounding tissue, referred to as interstitial tissue. The osteonal and interstitial tissues are separated by an interface called the cement line (CL), which is assumed to have a specific mineralization [24–27]. In reality, the area of cortical bone called interstitial tissue is composed of fragments of older osteons in which mineralization has highly increased with time [28]. This mixture of different fragments of osteons made them no more distinguishable between each other, thus random organization is observed. It has been suggested that osteocyte lacunae may have different properties within the osteon according to their distance to this CL [29–31]. Similarly, there are different types of lamellae that exist with different structural and mechanical properties [29,32–37]. This finding strongly suggests the evolution of biological activity during osteon formation and maturation of the tissue through mineralization.

Despite the differences in mineralization in the osteon compared to interstitial tissue, it is still difficult to identify osteons using standard characterization methods. In previous studies, analysis of osteons was mainly done manually using micro-radiography [38–40], histology [14,41], polarized light microscopy [42], or electron microscopy [13].

* Corresponding author.
E-mail address: peyrin@esrf.fr (F. Peyrin).

https://doi.org/10.1016/j.bone.2019.07.028
Received 28 January 2019; Received in revised form 23 July 2019; Accepted 24 July 2019
Available online 27 July 2019

These techniques provide 2D data of the osteonal system; however, bone has a complex 3D architecture [4,43,44].

Absorption Synchrotron Radiation Micro-Computed Tomography (SR-μCT) images allow for the visualization of contrast in osteons. To further segment osteons, a dedicated segmentation method had been proposed [45]. Hannah et al. also segmented osteons through 3D SR-μCT by averaging tomographic slices over 835 μm in order to enhance the sensitivity to density variations [30]. However, this method provides osteonal features that have the same geometry over 835 μm, which may not be representative of reality. In 2011, Cooper et al. showed that the phase contrast enhancement mode in 3D SR-μCT could be beneficial to the segmentation of osteons [46]. By placing the samples at some distance from the detector, one can enhance the edges around the borders of osteons. However, in their study, Cooper et al. only investigated the femoral diaphysis of a unique human donor, thus providing a good feasibility study, but insufficient data for quantitative analysis. Use both the phase contrast enhancement mode and quantitative phase retrieval improves contrast or osteons [11,25]. Nevertheless, despite increasing contrast, automatic segmentation of osteons remains challenging and there is currently very little 3D quantitative data.

Understanding of the bone remodelling process still remains a challenging topic, as it is a continuous process that occur throughout one's lifetime. It is now clearly assumed that such a process is initiated to replace a damaged area of the tissue in order to keep the whole organ healthy [20]. To better understand this process, the study of the osteonal and interstitial areas appears to be increasingly interesting, as it will provide a frozen picture of this renewal mechanism at a given time in the process. Investigating the properties of osteocyte lacunae [43], as well as mineralization on both sides of the cement line, will improve our knowledge of the relationship between bone 3D architecture and the role of osteons and cement lines in the orchestration of bone remodelling. In this study, we hypothesize that the cement line is a real structural and biological barrier that separates two different tissues having specific structural properties and that these properties reflect specific biological activity. Thus, the aim of this study is to assess the morphometric parameters of the osteonal system on eight human radii cortical bone samples using SR quantitative phase μCT to investigate the whether there is an observable and quantifiable difference in terms of osteocyte lacunae morphological organization between the osteonal and the interstitial tissue.

2. Materials and methods

2.1. Bone samples

In this study, bones samples were prepared from eight female donors (70.3 ± 13.7 y.o.; min/max: 50/91). The whole radii were extracted from fresh cadavers (French Ministry of Education and Research, authorization no. DC-2015-2357). The bones were provided by the Departement Universitaire d'Anatomie Rockefeller (Lyon, France) through the French program on voluntary corpse donation to science. No information regarding donor' disease or medication history was available, except for the absence of hepatitis and human immunodeficiency virus. The bones were frozen at −20 °C and covered with a saline-soaked gauze to maintain hydration until sample preparation.

2.2. Sample preparation

A rectangular sample was harvested from each radius using a low speed saw with a diamond-coated blade (ISOMET 4000, Buehler, USA). The samples were taken from the anterior region of the bone at nearly 70 mm from the proximal epiphysis in the middle area between the endosteum and the periosteum. This area corresponds to that used in a previous study involving the characterization of bone using guided waves [47]. Before performing SR-μCT imaging at the sub-micrometer scale, the samples were dehydrated to avoid blur artefact in the image. The preparation protocol used was the same as in a previous study [48], where this protocol was shown to produce artefactual microdamage of about 25% in trabecular bone. The samples were placed in acetone, rinsed in water, fixed in 70% ethanol solution and then dehydrated in a gradually increasing concentration of ethanol (from 70% to 100% spread over 48 h), thus minimizing damage or cracks. The final dimensions of the samples used for imaging were W = 2.02 ± 0.09 mm in the periosteum – endosteum direction, B = 1.00 ± 0.06 mm in the direction tangential to the bone section, and approximately 12.5 mm in the direction parallel to the long axis of the diaphysis in order to ensure proper clamping of the sample during images acquisition.

2.3. Synchrotron radiation micro-computed tomography (SR-μCT)

Image acquisition was performed on beamline ID19 at the European Synchrotron Radiation Facility (ESRF) in Grenoble, France. A “pink beam” filtered undulator radiation with an effective energy of 31 keV was used. It was obtained from a single-harmonic undulator U17.6 with an undulator gap set to 11.5 mm with a 5.6 mm-thick *Al* filter and a 1 mm diamond filter. Under these conditions, the FWHM was estimated to 6 keV. The detector was made of a scintillator screen, a visible light microscope, and a CCD camera. The effective pixel size on the detector was 0.7 μm, and the detector's field of view was $1.4 \times 1.4\,mm^2$. A total of 2000 projection images were recorded over a rotation of 360°, with a counting time of 0.3 s resulting in a scan time of 14 min for each sample. The sample-to-detector distance was set to 40 mm to record phase contrast. The images were reconstructed with and without phase retrieval. Phase retrieval was performed using Paganin's method [49], with the value of δ/β set at 572. The volume reconstructions for the eight samples were performed using a filtered-back projection algorithm yielding 3D images with 2048^3 voxels. The size of the bone samples' Volume Of Interest (VOI) was approximately $1 \times 1.4 \times 1.4\,mm^3$, with the 1 mm dimension corresponding to thickness B of the sample (cf. 2.2) (Fig. 1).

2.4. Image segmentation

Image analysis consisted of an investigation of osteonal canals, osteons, lacunae, and micro-cracks within the VOIs.

2.4.1. Segmentation of the canals

Segmentation of these different structural features was performed automatically on the $1 \times 1.4 \times 1.4\,mm^3$ volumes using the same method, as stated in a previous study [43].

We first separated the osteonal canals from other porosities. A bone mask was generated by applying a median filter to the volume and a threshold using the Otsu method. Lacunae and micro-cracks (< 30 μm) were removed by applying a threshold on the size of each object after performing a connected component analysis. The canal mask was then considered as the complement of the bone mask.

2.4.2. Segmentation of the osteons

Osteon segmentation was performed manually using Avizo software (Thermal Fischer Scientific) on the phase-retrieved volume. For each osteon, the interface between osteonal and interstitial tissue was delineated in slices perpendicular to the main axis of the bone diaphysis. The segmented objects were defined by all of the pixels within the delineated interface. An interpolation tool provided by the software was used to avoid performing contouring on each slice. The interpolation step depended on the shape evolution of each osteon, from 5 μm when the osteon's shape changed considerably in relation to the slice (for example, when two osteons joined together) to 50 μm when the shape of the osteons was almost constant along the diaphysis (almost cylindrical). A complete segmentation of the VOI provides a

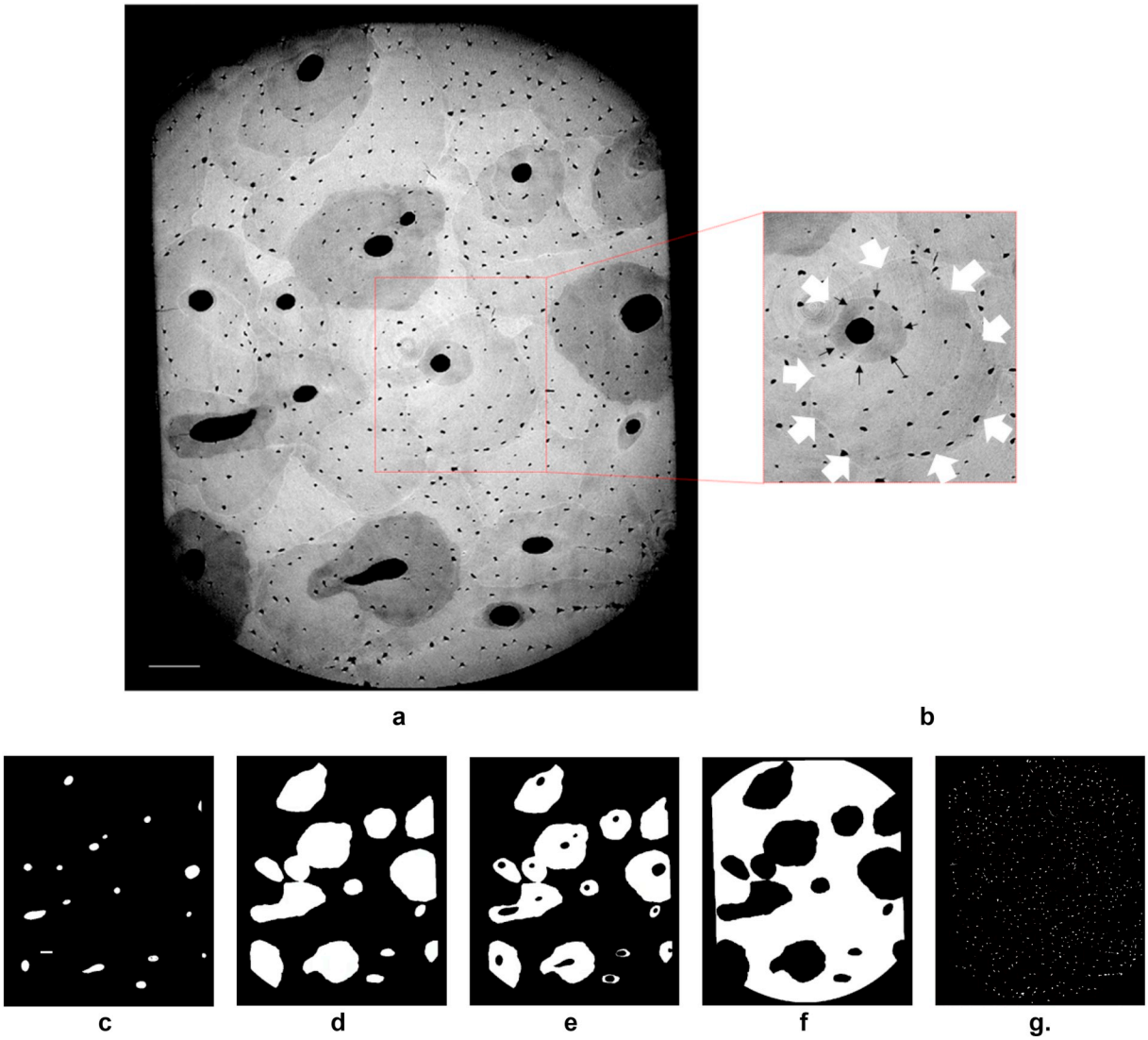

Fig. 1. a.: VOI phase contrast slice from a radius sample of a female donor (50 y.o.), b.: Cropped image of a single osteon. Note the two interfaces (white and black arrows). The chosen interface is the one closer to the canal pointed by the black arrows. Following figures: binary-segmented volumes of c.: Haversian or Volkmann canals mask, d.: total osteon mask, e.: osteons mask (canals subtracted), f.: interstitial mask, g.: Lacunae and micro-cracks mask. Scale bars = 100 µm. Note the distinct osteons around the canals in darker gray than the surrounding interstitial tissue.

binary volume with all of the segmented objects. Then the canals mask was subtracted from this binary volume in order to only have the osteons mask and its complementary volume, which would be the interstitial tissue mask (Fig. 1). A similar procedure has been applied by Maggiano et al. [50].

Osteons can be distinguished from interstitial tissue due to their differences in gray levels, which correspond to their differences in mineralization, which is enhanced in a X-ray phase CT (Fig. 1). For some cases, two different osteons could be seen around a single canal, showing that bone remodelling is a dynamic process. In such a case, the osteon that was closer to the canal (meaning the younger osteon (Fig. 1b)) was chosen.

2.4.3. Segmentation of lacunae and micro-cracks

Lacunae and micro-cracks were then segmented automatically using the following process. First, hysteresis thresholding was applied to the volume within the bone mask, resulting in a binary volume containing both lacunae and micro-cracks (Fig. 1g) [43]. From this volume, a connected component analysis was performed to label each object (either lacuna (Lc) or micro-crack (µCr)), and geometric descriptors of these objects were calculated [3]. In this study, each object is considered as an ellipsoid with three main axes (L1, L2, and L3 in µm). Lacunae and micro-cracks were then separated into two classes of objects distinguished by morphometric criteria such as volume (V in μm^3), thickness (Th in µm), aspect ratios or Structural Model Index (SMI), or Euler number (χ) [51]. The calculations for these parameters are given in [3,43]. The micro-crack criteria used in the current study were inspired by the criteria used in [43], with some slight differences. Table 1 gives a summary of the criteria used for the segments for only osteocytes lacunae or micro-cracks.

After the automatic segmentation, manual refinement was performed within the micro-cracks volume to eliminate any artefacts, such as large lacunae that look like micro-cracks.

2.5. Image analysis

The nomenclature for the analysed parameters in the current study were defined according to bone histomorphometry standardization [52,53].

2.5.1. Canals analysis

Osteonal canals –(On.Ca) were analysed using CTAn (CT Analyser

Table 1
Inclusion morphometric criteria for the segmentation of the osteocyte lacunae (Lc) or of the micro-cracks (μCr) [43].

Osteocytes lacunae	Micro-cracks
Lc.V > 82 μm^3 and Lc.V < 10,000 μm^3	μCr·V > 500 μm^3
Lc.L1/Lc.L3 < 15 and Lc.L2/Lc.L3 < 8	μCr.L1μCr.Th > 15, μCr.L2/μCr.Th > 11 and μCr.L3/μCr.Th > 1.5
Lc.SMI > 1.6	μCr.Th < 4
0 < Lc.χ < 2	μCr.SMI < 2.5

Software V 1.14.4, Skyscan NV, Kontich, Belgium). On these VOIs, the canal volume fraction On.Ca·V/TV (%) was quantified. Total Volume (TV, in mm^3) was measured by adding the voxels of the canal mask On.Ca·V (mm^3) and those of the bone mask BV (mm^3). Mean canal diameter On.Ca.Dm (μm) was also measured as the value of the maximal fitting sphere within the structure [54].

2.5.2. Osteon analysis

Osteons were also analysed using CTAn (CTAnalyser Software V 1.14.4, Skyscan NV, Kontich, Belgium). Osteonal volume On.V (mm^3) was measured as the sum of the voxels of the osteonal mask. Osteonal volume fraction was measured both as a function of total volume On.V/TV (%) and as a function of bone volume On.V/BV (%) because they are present in bone tissue. Diameter On.Dm (μm) was also measured using the same method as that for the canals and thus was included the canal. Finally, the total perimeter of the osteonal system, On.Pm (mm), was calculated as the average value of the perimeter measured slice by slice. This value is an estimation of the total length of the cement line on each slice. For the latter, the volume including both osteons and canals was used (Fig. 1d).

The volume of the interstitial tissue It.V (mm^3) was also calculated.

2.5.3. Lacunae and micro-cracks analysis

Regarding lacunae, the dimensions of the three main axes of the best-fitting ellipsoid were analysed for Lc.L1, Lc.L2, and Lc.L3 (μm) [3,43]. The ratios Lc.L1/Lc.L2 and Lc.L1/Lc.L3 were also computed. Their volume fraction Lc.V/BV (%) and density Lc.N/BV (mm^{-3}) were quantified. These parameters were measured with respect to Bone Volume (BV).

To analyse the differences between the osteonal and interstitial tissue, the lacunae included in the osteonal volume and in the interstitial volume were separated, and their properties were calculated separately. For volume fraction and density, lacunar volume and number were divided by either osteonal volume (for lacunae within osteons) or interstitial volume (for the other lacunae) (Lc.V/On.V (%), Lc.N/On.V (mm^{-3}) or Lc.V/It.V (%), Lc.N/It.V (mm^{-3}), respectively).

Micro-cracks volume fraction μCr·V/BV (%) was also measured.

As for the lacunae, micro-cracks within the osteons or within the interstitial tissue were then analysed separately and provided the following quantities: μCr·V/On.V (%) or μCr·V/It.V (%).

2.5.4. Bone mass density

Bone mass density, ρ (g·cm^{-3}) was calculated from the reconstructed image using the following equation [25]:

$$\rho\ (g{\cdot}cm^{-3}) = \frac{\delta}{\beta}{\cdot}\frac{\mu.\ 10^{-1}}{4\pi.\ 1.3.\ \lambda}\ with\ \frac{\delta}{\beta} = 572\ (cf.\ 2.3), \quad (1)$$

where μ (mm^{-1}) is the linear attenuation coefficient obtained directly as the output of the reconstructed software, and λ (Å) is the wavelength of the X-ray beam (λ = 0.400 Å at 31 keV).

Bone mass density was calculated for the complete volume of bone (BV), osteonal volume (On.V), and interstitial volume (It.V) excluding all porosities (canals, lacunae or micro-cracks).

2.5.5. Distribution of the lacunar properties with respect to the cement lines (CL)

In order to analyse the distribution of the lacunae's properties on both sides of the CL, a CL mask was first created by calculating the morphological derivate of the osteons mask (i.e., subtracting the dilated and eroded images). We then calculated the Euclidian distance map of the CL and the Euclidian distance map from the osteonal canals' boundaries, which provide a volume of the shortest distance to the CL and a volume of the shortest distance to the canals. For each lacuna in an osteon, the ratio between its distance to the canal boundaries (value for the canal distance map) and the distance between the canal and the CL (value for the canals mask's distance map + value for the CL's distance map) was assigned at its barycentre. A value of 1 corresponds to a lacuna that is at the cement line, whereas a value of 0 is at the canal boundary. For each lacuna within the interstitial tissue, the ratio between its distance to the canal (value for the canals mask's distance map) and the distance between the canal and the CL (value for the canals mask's distance map – value for the CL's distance map) was assigned at its barycentre. A value of 1 corresponds to a lacuna that is on the CL, a value of 2 corresponds to a point at which the distance to the canal is twice that of the distance from canal boundary to CL. In the following, the value assigned to each lacuna is called the normalized distance.

The distance maps were then partitioned into bins of 0.02. For example, the first bin is composed of voxels with a value of a distance ratio ranging from 0 to 0.02. Lacunae parameters were averaged on each of these bounded volumes. Lacunar density was also measured by dividing the number of lacunae within the bin (N.Lc) by the number of voxels within the bin (Bin.V (mm^3)). Voxels included in the canals mask were not considered in these bins, because there was no lacuna found in these canals.

For the bone mass density, the relative difference (Δρ in %) between the values of ρ within the bin and the mean value obtained for the bone volume was investigated.

Values from 0 to 1 correspond to osteons and values from 1 to 2 correspond to interstitial tissue (see Fig. 3).

2.6. Statistical tests

A non-parametric Friedman test for independent samples was applied before applying a Wilcoxon test for paired samples using StatView (SAS Institute Inc., USA) to analyse differences between osteonal and interstitial tissue. Correlations were analysed by measuring the Spearman coefficient. Results with p-value < 0.05 were considered as significant.

The Spearman's coefficient between the osteonal morphometric parameters and osteonal canals, lacunae, and micro-cracks parameters was measured.

3. Results

Fig. 2 shows the 3D rendering of the VOI obtained from the radius of a female donor after segmentation (50 y.o.).

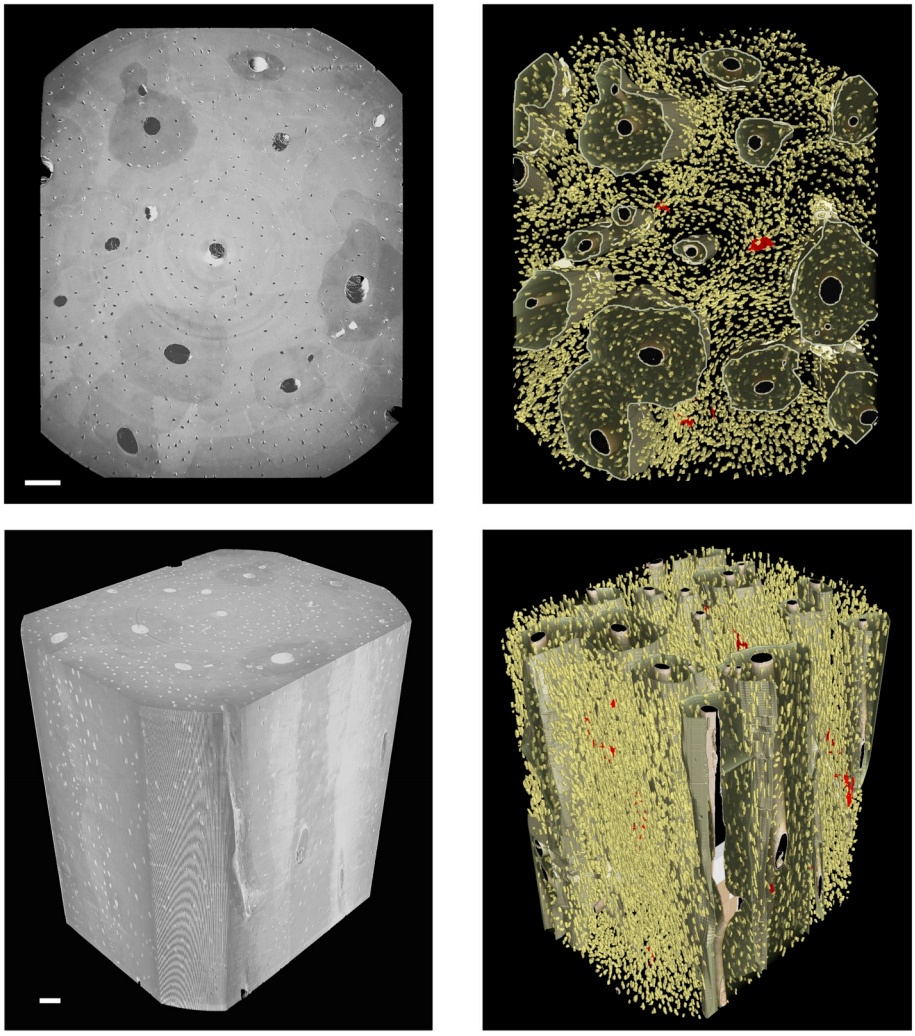

Fig. 2. 3D rendering of the VOI from a donor (50 y.o.) under two orientations. a. phase contrast; b.: segmented volume. Note in olive-green the osteons, in yellow the osteocytes lacunae and in red the micro-cracks. Scale bar = 100 µm. (For interpretation of the references to colour in this figure legend, the reader is referred to the web version of this article.)

3.1. Canals analysis

Morphometric values measured for Haversian canals are given in Table 2.

3.2. Osteon analysis

Morphometric values obtained for osteonal system are given in Table 3.

3.3. Lacunar and micro-cracks analysis

Tables 4 and 5 show lacunar and micro-cracks morphometric parameters, respectively, for the total volume, in osteons and in interstitial tissue.

Table 2
Morphometric parameters of Haversian canals.

Morphometric parameters	Average (SD)
On.Ca·V/TV (%)	4.5 (2.1)
On.Ca.Dm (µm)	64.7 (23.1)

Table 3
Morphometric parameters of osteons.

Morphometric parameters	Average (SD)
On.V/TV (%)	40.9 (6.8)
On.V/BV (%)	43.2 (8.4)
On.Dm (µm)	184.0 (13.3)
On.Pm (mm)	5.6 (0.8)

There were significant differences between the lacunar properties in osteons and those in the interstitial tissue. Lacunar density is 11.8% higher in the osteonal tissue compared to the interstitial tissue. Lc.L1 is 6.4% higher in the interstitial tissue resulting in a Lc.L1/Lc.L2 10% higher in the interstitial tissue and a Lc.ρ_1 15.8% higher in osteonal tissue.

85% of the micro-cracks were observed within interstitial tissue

3.4. Bone mass density

Table 6 shows bone mass density values obtained for bone volume, osteonal and interstitial volumes. There was a significant difference measured between osteonal and interstitial volumes, with an osteonal

Table 4
Lacunar morphometric parameters. Note that for the osteon and interstitial tissue, BV = On.V or It.V, respectively (Average (SD)).

Morphometric parameters	Bone	Osteon	Interstitial tissue
Lc.V/BV (%)	1.2 (0.1)	1.1 (0.4)	1.3 (0.1)
Lc.N	32,609	15,035	17,574
Lc.N/BV (mm^{-3})	**19,621 (2171)**[a]	**20,832 (2522)**	**18,621 (1682)**
Lc.L1 (μm)	**25.3 (2.5)**[a]	**24.5 (2.0)**	**26.2 (3.3)**
Lc.L2 (μm)	10.9 (0.7)	11.22 (1.0)	10.8 (0.6)
Lc.L3 (μm)	5.3 (0.2)	5.3 (0.2)	5.3 (0.3)
Lc.L1/Lc.L2	**2.3 (0.3)**[a]	**2.2 (0.2)**	**2.4 (0.3)**
Lc.L1/Lc.L3	4.8 (0.5)	4.7 (0.4)	5.0 (0.8)

[a] + bold: Significant difference between osteonal and interstitial tissue (p-value < 0.05).

Table 5
Micro-cracks morphometric parameters. Note that for the osteon and interstitial tissue, BV = Ost.V or Inter.V, respectively (Average (SD)).

Morphometric parameters	Bone	Osteon	Interstitial tissue
μCr·V/BV (% × 10^3)	**8.3 (7.4)**[a]	**2.4 (2.9)**	**12.2 (10.2)**

[a] + Bold: Significant difference between osteonal and interstitial tissue (p-value < 0.05).

Table 6
Bone mass density. Note that for the osteon and interstitial tissue, BV = Ost.V or Inter.V, respectively (Average (SD)).

Morphometric parameters	Bone	Osteon	Interstitial tissue
ρ ($g{\cdot}cm^{-3}$)	**1.68 (0.04)**[a]	**1.62 (0.06)**	**1.72 (0.03)**

[a] + Bold: Significant difference between osteonal and interstitial tissue (p-value < 0.05).

value of mass density 5.6% lower.

3.5. Correlations

Table 7 gives the Spearman's coefficient between morphometric parameters of osteons and the other structural features.

A significant correlation was observed between the canal and osteon volume fraction.

Regarding he osteocyte lacunae, there were significant correlations between the osteonal volume fraction On.V/BV and Lc.L1, Lc.L1/Lc.L2 and Lc.ρ_1. The osteonal perimeter On.pm also has a strong correlation with Lc.N/BV, Lc.L1, Lc.L1/Lc.L2 and Lc.L1/Lc.L3. There was no significant correlation for osteonal diameter On.Dm.

Finally, the micro-cracks volume fraction is significantly correlated with the osteonal volume fraction, but there was no correlation between crack volume fraction and osteonal diameter or perimeter.

There was no correlation between any of the morphometric parameters and the age of donors.

3.6. Distribution of the lacunar properties with respect to the CL

Fig. 3 gives an example of the distributions of lacunae properties within the osteon expressed as a function of the normalized distance to the canal. Fig. S1 in the supplementary materials shows the gathered data for all the donors. These curves are reported from one female donor (50 y.o.), but they are representative of all of the distributions obtained for the eight donors. For all of the parameters, variation is seen within the osteon and almost no variation is observed in the interstitial tissue.

Lacunar density (Fig. 3a) increases by almost 100%, from 15,000 to 30,000 mm^{-3}, near the cement line before decreasing at the cement line. The bell part of the curve ranges from 0.75 to 1.

Table 7
Spearman's coefficient between osteonal tissue and Haversian canals, lacunar and micro-cracks morphometric parameter.

	Haversian canals	
	On.Ca·V/TV	On.Ca.Dm
On.V/BV	**0.88***	0.67
On.Dm	0.47	0.48
On.Pm	0.56	0.33

	Osteocytes lacunae						
	Lc.V/BV	Lc.N/BV	Lc.L1	Lc.L2	Lc.L3	Lc.L1/Lc.L2	Lc.L1/Lc.L3
On.V/BV	0.17	0.60	**−0.71***	0.31	−0.24	**−0.91***	−0.57
On.Dm	−0.41	−0.24	0.05	−0.17	−0.40	0.04	0.08
On.Pm	0.31	**0.83***	**−0.95***	0.07	0.19	**−0.81***	**−0.91***

	Micro-cracks
	μCr·V/BV
On.V/BV	**−0.74***
On.Dm	0.18
On.Pm	−0.69

* p-Value < 0.05.

The variation for Lc.L1 (Fig. 3b) in the osteon is a bell curve that ranges between the canal and the CL, with a maximum value at the middle of the osteon and drops close to the CL. The values at the canal and at the CL are nearly the same.

Lc.L2 (Fig. 3c) and Lc.L3 (Fig. 3d) show the same kind of variation, with a maximum value near the CL and a slight decrease before the canal. For Lc.L3, the decrease increases near the canal, from a distance ratio of 0.15 to 0.

The aspect ratio Lc.L1/Lc.L2 (Fig. 3e) has the same kind of variation as Lc.L1, thus highlighting the higher variation of Lc.L1 than Lc.L2.

Regarding Δρ (Fig. 3f), the interesting point is an increase at the CL.

4. Discussion

This study investigated the 3D properties of the osteonal system in human cortical bone samples extracted from the radius of eight female donors using SR-μCT. To the best of our knowledge, this is the first time that such a data set on bone microstructure has been obtained.

Previous data on cortical bone osteons were mainly obtained using 2D techniques, which makes it difficult to compare to our results. In 2000, Yeni et al. performed histological analyses on samples harvested from femoral necks [41]. The values of canal and osteonal volume fractions found in the current study are of the same order of magnitude as the values of canal and osteonal area fractions found by Yeni et al. (4.1 ± 2.1%/43.2 ± 8.4% in the current study, 6.75 ± 2.62%/48.17 ± 14.57%, in [41], respectively, for the canal/osteonal fractions). In the previous study, analyses were performed on human femoral neck samples compared to the human radii in the current study, which can partly explain the slight differences. In the same way, the diameters of the Haversian canals and the osteons obtained in the current study in 3D (On.Ca.Dm = 64.7 ± 23.1 μm/On.Dm = 184.0 ± 13.3 μm) are of the same order of magnitude as the previous results found in 2D using histology (On.Dm = 193.35 ± 10.98 μm in [14]) or scanning electronic microscopy (On.Ca.Dm = 69.71 ± 35.95 μm/On.Dm = 156.31 ± 51.09 μm in [24]). These two previous studies investigated human femoral diaphyses [14,24]. Since the authors previously found evidence of significant differences in the canal's architecture in the radius compared to the

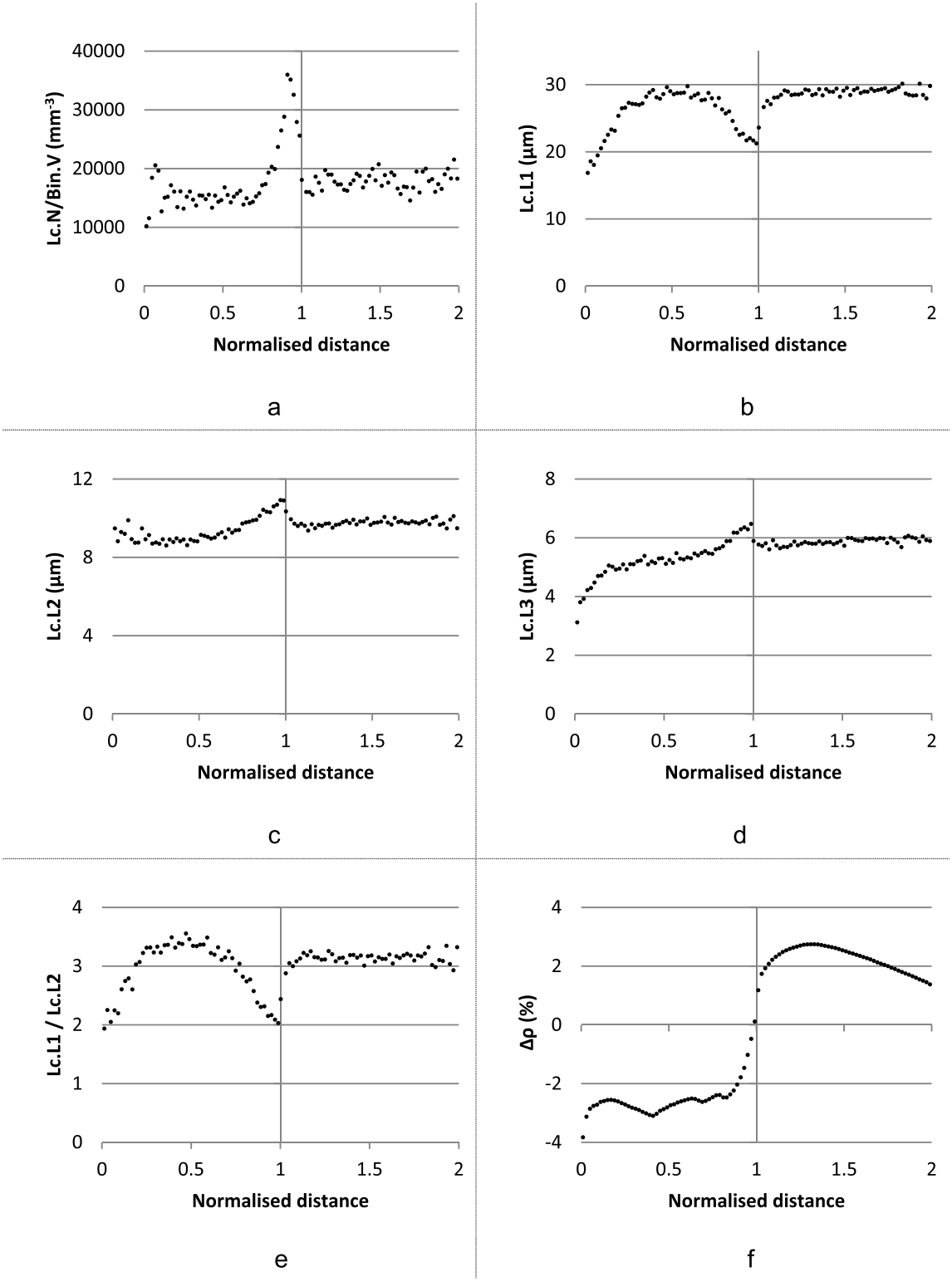

Fig. 3. Distributions of the lacunar morphometric parameters from the CL for a radius sample of a female donor (50 y.o.). Values between 0 and 1 correspond to the osteon; the CL is at the ratio distance 1. a.: lacunar density in each bin, b.: Lc.L1, c.: Lc.L2, d.: Lc.L3, e. Lc.L1/Lc.L2 and f.:Δρ.

femoral diaphysis [43], the differences in osteons can be expected at these two anatomical locations.

It is interesting to observe that the volume fraction of osteons is correlated with the volume fraction of the osteonal canals. This correlation highlights that tissue with a high amount of Haversian porosity will present a higher amount of osteons than tissue with a lower Haversian porosity. This result is consistent, since the osteons arise through a bone remodelling process that is initiated at the osteonal canals. When the signal is sent to remodel a damaged area, osteoclasts initiate the resorption step along osteonal canals. Once this resorption step is concluded, the cement line is deposited, and bone deposition by osteoblasts initiates along the bone surface available in the osteonal canals [16,18,55]. Bone tissue with a higher amount of Haversian canals will present more sites for the initiation of the remodelling process.

Still no correlation was found between the osteonal and Haversian canals diameters (On.Dm and On.Ca.Dm). This is consistent with the way in which the bone remodelling process is undergone. In the early stage of the remodelling process, osteoclasts first initiate resorption, which yield to the creation of a cutting cone, and then this cutting cone is widened in order to resorb all of the damaged tissue. The formation of bone is then initiated on the wall of the cutting cone. This process shows that the size of the cutting cone will vary all along its length [16,56].

The averaged values for the osteocytes lacunae obtained have already been discussed in [43]. The values are slightly different because, in the current study, a larger volume of interest was analysed (e.g., Lc.L1 = 25.3 (2.5) μm in the current study and Lc.L1 = 25.7 (2.2) in [43]). We found significant differences in the lacunae density, lacunae main length, and anisotropy between the osteonal and interstitial tissues. To the best of our knowledge, there is no equivalent data in the literature. Some studies have nevertheless been performed to assess the lacunae morphometric parameters within the osteonal tissue alone, without investigating the differences with the interstitial tissue [29–31,57,58]. We can state that the significant differences between properties of the osteonal and interstitial tissues arise mainly due to variations observed within osteons. For example, lacunar density is nearly constant in osteonal tissue close to the canal or in interstitial tissue, but a high peak is observed close to the CL. This peak increases the averaged value measured in the osteonal tissue. Similar results regarding variation in lacunar density have already been observed in the past, both in 2D [31] and in 3D [30]. In these studies, a variation of lacunar density was measured as a function of the distance to the cement line of the osteon. In particular, a decrease in this density was measured as we move away from the cement line. However, these studies were performed on only one subject, either in 2D [31] or in 3D, assuming a constant contour along 835 μm [30]. The current study involves 3D VOIs obtained from eight donors involving an average of 32,609 lacunae on each VOI. Moreover, the segmentation of osteons is more realistic than in that of [30]. It is known that osteocytes are former osteoblasts that are embedded within the bone matrix after deposition of tissue [59,60]. The bone deposition rate by the osteoblast during the bone remodelling process decreases from the beginning until the end of the deposition process, and the osteocytes density was related to the deposition rate [61–64]. As the CL is the interface at which bone deposition begins [65], the higher osteocyte lacunae density near this CL may reflect the higher activity of these osteoblasts at the beginning of the bone remodelling process. In a previous study, Repp et al. investigated the spatial heterogeneity of the canaliculi within the osteons [66]; the canaliculi are small canals < 0.40 μm in diameter that connect the osteocytes between them and form the lacuna-canalicular network [67]. Their results showed that the density of canaliculi vary from the canal surface to the cement lines in the opposite way compared to the lacunae density in the current study, the density of canaliculi is higher near the Haversian canal surface [66]. It would be interesting to investigate the relationships between the canaliculi density and osteocytes morphometric parameters measured in the current study. However, the parameters used for the imaging protocol in the current study do not allow the investigation of such features.

In a previous study, Atkinson et al. also observed that the lacunae near the CL were larger than the lacunae near the canal [57]. As their study was performed in 2D and perpendicular to the osteon, the long axis of lacunae that they consider corresponds to Lc.L2 measured in the current study [3]. Our results show a slight increase of Lc.L2 from the canals boundary to the CL (Fig. 3). In a previous study, Ardizzoni observed a relation between a decrease in the thickness of the lamellae that made bone tissue from the CL to the canal and lacunae size [29]. He assumed that lamellae are thinner near the canal because of the decrease in the size of osteocytes and, more specifically, the decrease in the size of the former osteoblasts before their differentiation in osteocytes. Our results regarding Lc.L1 and for Lc.L1/Lc.L2 and Lc.ρ_1 are original, as most previous studies were performed in 2D on a section perpendicular to the osteon, whereas osteocyte lacunae are oriented parallel to the osteon [3]. Considering the previous hypothesis that osteocytes dimensions have an influence on bone deposition, these results strongly suggest that bone formation goes through different steps between the start of the deposition at the cement line until the end of the process, as reflected by the bell curves in Fig. 3. The importance of the CL in terms of lacunar system organization is also highlighted due to the correlations found between osteonal and lacunar parameters, more specifically with the osteons perimeter (see Table 7).

The lack of variation in the lacunar geometry observed within the interstitial tissue uncovers several questions. One explanation could be that, since the interstitial tissue is in reality a mixture of fragments of older osteons, the possible variations of lacunar geometry properties could be averaged when considering only the distance to the cement line. Another explanation for the differences in the lacunar geometry between the osteonal and interstitial tissue, but also regarding the variation within one osteon, could be found in the perilacunar remodelling that might occur in the local environment of the osteocytes, meaning that remodelling (resorption/deposition of bone tissue) might still occur after the differentiation of osteoblasts into osteocytes. This topic has long been a topic of discussion, but recent studies demonstrate that such a process occurs in bone tissue [67–72]. Under this hypothesis, the geometry of the osteocyte lacunae, once embedded in the bone matrix, can evolve over time [73]. This perilacunar remodelling can occur either in the osteon or in the interstitial tissue.

The micro-crack volume fraction obtained in the current study is larger than the value found in a previous study on smaller VOIs ($8.3 \times 10^{-3} \pm 7.4 \times 10^{-3}$% in the current study, $24.32 \times 10^{-3} \pm 17.66 \times 10^{-3}$% in [43]). The differences might be explained by the slight difference in the choice of the morphometric criteria and manual refinement of the segmentation that was performed in the current study. This refinement was not performed in [43] because of the large number of analysed volumes. Moreover, in the current study, the size of the VOIs is much larger than in the previous study. Still, the value of μCr·V/BV is very small. In the current study, we observed a large difference of 75% between the osteonal and interstitial tissue. This is in accordance with previous results showing that micro-cracks are mainly initiated in the interstitial tissue that is more mineralized, whereas cement lines act as barriers to these cracks [8,74,75]. Schaffler et al. also found that 85% of the micro-cracks included in bone are observed in the interstitial tissue. This observation might be explained by the difference in mineralization between the interstitial and the osteonal tissue. A more mineralized tissue (i.e. a stiffer tissue [76]) is indeed a preferential area for the initiation and the propagation of cracks [77].

The mass density values obtained in the current study are comparable to the bone mass density data obtained in a previous study from our group investigation of cortical bone sample using SR-μCT [25]. The difference in the bone mass density found between osteonal and interstitial tissue was expected, since osteon is a younger tissue that arises from the remodelling process [21–23,28]. However, this difference is small (5.6%), which explains the difficulty in automatically segmenting osteons from interstitial tissue. A study by Langer et al. revealed a higher density at the CL that was not observed in the current study [25]. In this previous study, the resolution was higher than in the current study (pixel size of 60 nm in [25] and 0.7 μm in the current study). This higher resolution allows for better visualization of these cement lines, as they are interfaces that are < 5 μm in thickness [55].

It should be noted that the current study has been performed on the radius of eight female donors aged from 50 to 91 y.o. It is widely known that anatomical location [43,78], gender [79,80], and age [14,81] influence bone microstructure. This means that the results obtained correspond to a specific population and cannot be generalized to a larger population of younger or male donors.

It is also worth noting that, in such cortical bone samples, what is

called interstitial tissue is composed of different fragments of old osteonal tissue that, with time, have reached a higher level of mineralization and are less distinguishable, as seen in Fig. 1. The results of the current study were obtained by selecting only the smaller osteon adjacent to each canal, referring to the smaller osteon in the case that there are two concentric osteons. This means that our osteon data set represents a population of new osteons (see Fig. 1b).

The author acknowledge that the cutting and preparation protocols are likely to introduce micro-cracks. The influence of ethanol drying procedure as used in the current study was shown to induce artefactual micro-cracks of about 25% (of 100% detected) when analysed using optical microscopy [48]. As this past study was done on trabecular and not cortical human bone, the proportion of pre-existing and induced micro-cracks cannot be elucidated in the present study but may be in a similar range. The size of the VOIs used in the current study can also be considered as small ($1 \times 1.4 \times 1.4\,mm^3$). A previous study revealed that there was no difference between osteonal canals morphometric parameters measured on two contiguous VOIs of $1 \times 1.4 \times 1.4\,mm^3$, as in the current study. Even if the osteonal canals are smaller than osteons, they are correlated (see Table 7). This conforms to the results obtained in the current study on the osteonal system.

The number of donors used in this study is small (eight donors). In a previous study, we performed a total of 48 scans on paired femoral diaphyses, femoral necks, and radial diaphyses both on control and fractured VOIs [12,43]. But as the manual segmentation of the osteons is highly time consuming, the authors chose first to perform the investigation on a sub-population of these 48 scans. Regarding the results obtained, it is obvious that enlarging the study to include femoral diaphyses and necks would be of great interest to assess the influence of anatomical location. Furthermore, the investigation of the influence of the osteonal system on bone crack propagation mechanisms would also be of great interest to better understand the bone fracture process.

5. Conclusions

The current study investigated the osteonal systems of eight female donor radii in three dimensions. Novel results were obtained regarding the morphometric parameters of the osteons. The morphometric parameters of osteocyte lacunae appear to follow a specific distribution between the Haversian canal surface and the cement line. The importance of cement lines in bone architecture has been highlighted. The structural differences on both sides of the cement lines strongly suggest a different biological activity between osteonal and interstitial tissue.

Supplementary data to this article can be found online at https://doi.org/10.1016/j.bone.2019.07.028.

Declaration of Competing Interest

The authors declare no conflict of interest. The funding sponsors had no role in the design of the study; in the collection, analyses, or interpretation of data; in the writing of the manuscript, and in the decision to publish the results.

Acknowledgments

The authors acknowledge the ESRF ID19 staff for his support for synchrotron data acquisition during the experiment MD923. This work was partly funded by the LabEx PRIMES, France (ANR-11-LABX-0063) within the program “Investissements d'Avenir”, France (ANR-11-IDEX-0007). This study was also partly funded by the Région Auvergne-Rhône-Alpes, France (14-011125-01). This work was also done in the context of the ANR project MULTIPS (ANR-13-BS09-0006) and of the project France Life Imaging (ANR-11-INBS-0006). '

References

[1] E. Seeman, P.D. Delmas, Bone quality–the material and structural basis of bone strength and fragility, N. Engl. J. Med. 354 (2006) 2250–2261, https://doi.org/10.1056/NEJMra053077.
[2] J.Y. Rho, L. Kuhn-Spearing, P. Zioupos, Mechanical properties and the hierarchical structure of bone, Med. Eng. Phys. 20 (1998) 92–102, https://doi.org/10.1016/S1350-4533(98)00007-1.
[3] P. Dong, S. Haupert, B. Hesse, M. Langer, P.J. Gouttenoire, V. Bousson, F. Peyrin, 3D osteocyte lacunar morphometric properties and distributions in human femoral cortical bone using synchrotron radiation micro-CT images, Bone 60 (2014) 172–185, https://doi.org/10.1016/j.bone.2013.12.008.
[4] Y. Bala, E. Lefevre, J.P. Roux, C. Baron, P. Lasaygues, M. Pithioux, V. Kaftandjian, H. Follet, Pore network microarchitecture influences human cortical bone elasticity during growth and aging, J. Mech. Behav. Biomed. Mater. 63 (2016) 164–173, https://doi.org/10.1016/j.jmbbm.2016.05.018.
[5] G.E. Fantner, T. Hassenkam, J.H. Kindt, J.C. Weaver, H. Birkedal, L. Pechenik, J. a Cutroni, G. a G. Cidade, G.D. Stucky, D.E. Morse, P.K. Hansma, Sacrificial bonds and hidden length dissipate energy as mineralized fibrils separate during bone fracture, Nat. Mater. 4 (2005) 612–616, https://doi.org/10.1038/nmat1428.
[6] R. Voide, P. Schneider, M. Stauber, P. Wyss, M. Stampanoni, U. Sennhauser, G.H. Van Lenthe, R. Müller, Time-lapsed assessment of microcrack initiation and propagation in murine cortical bone at submicrometer resolution, Bone 45 (2009) 164–173, https://doi.org/10.1016/j.bone.2009.04.248.
[7] G.C. Reilly, Observations of microdamage around osteocyte lacunae in bone, J. Biomech. 33 (2000) 1131–1134, https://doi.org/10.1016/S0021-9290(00)00090-7.
[8] D.B. Burr, M.B. Schaffler, R.G. Frederickson, Composition of the cement line and its possible mechanical role as a local interface in human compact bone, J. Biomech. 21 (1988) 939–945, https://doi.org/10.1016/0021-9290(88)90132-7.
[9] Y.N. Yeni, C.U. Brown, Z. Wang, T.L. Norman, The influence of bone morphology on fracture toughness of the human femur and tibia, Bone 21 (1997) 453–459, https://doi.org/10.1016/S8756-3282(97)00173-7.
[10] O.L. Katsamenis, T. Jenkins, P.J. Thurner, Toughness and damage susceptibility in human cortical bone is proportional to mechanical inhomogeneity at the osteonal-level, Bone 76 (2015) 158–168, https://doi.org/10.1016/j.bone.2015.03.020.
[11] U. Wolfram, J.J. Schwiedrzik, M.J. Mirzaali, A. Bürki, P. Varga, C. Olivier, F. Peyrin, P.K. Zysset, Characterizing microcrack orientation distribution functions in osteonal bone samples, J. Microsc. 00 (2016) 1–14, https://doi.org/10.1111/jmi.12440.
[12] R. Gauthier, M. Langer, H. Follet, C. Olivier, P.-J. Gouttenoire, L. Helfen, F. Rongiéras, D. Mitton, F. Peyrin, Influence of loading condition and anatomical location on human cortical bone linear micro-cracks, J. Biomech. (2019), https://doi.org/10.1016/j.jbiomech.2019.01.008.
[13] M. Granke, A.J. Makowski, S. Uppuganti, J.S. Nyman, Prevalent role of porosity and osteonal area over mineralization heterogeneity in the fracture toughness of human cortical bone, J. Biomech. 49 (2016) 2748–2755, https://doi.org/10.1016/j.jbiomech.2016.06.009.
[14] A. Bernhard, P. Milovanovic, E.A. Zimmermann, M. Hahn, D. Djonic, M. Krause, S. Breer, K. Püschel, M. Djuric, M. Amling, B. Busse, Micro-morphological properties of osteons reveal changes in cortical bone stability during aging, osteoporosis, and bisphosphonate treatment in women, Osteoporos. Int. 24 (2013) 2671–2680, https://doi.org/10.1007/s00198-013-2374-x.
[15] R.F.M. van Oers, R. Ruimerman, E. Tanck, P.A.J. Hilbers, R. Huiskes, A unified theory for osteonal and hemi-osteonal remodeling, Bone 42 (2008) 250–259, https://doi.org/10.1016/j.bone.2007.10.009.
[16] N.E. Lassen, T.L. Andersen, G.G. Pløen, K. Søe, E.M. Hauge, S. Harving, G.E.T. Eschen, J.M. Delaisse, Coupling of bone resorption and formation in real time: new knowledge gained from human Haversian BMUs, J. Bone Miner. Res. 32 (2017) 1395–1405, https://doi.org/10.1002/jbmr.3091.
[17] J.M. Delaisse, The reversal phase of the bone-remodeling cycle: cellular prerequisites for coupling resorption and formation, Bonekey Rep 3 (2014) 1–8, https://doi.org/10.1038/bonekey.2014.56.
[18] A.M. Parfitt, Osteonal and hemi-osteonal remodeling: the spatial and temporal framework for signal traffic in adult human bone, J. Cell. Biochem. 55 (1994) 273–286, https://doi.org/10.1002/jcb.240550303.
[19] D.B. Burr, R.B. Martin, M.B. Schaffler, E.L. Radin, Bone remodeling in response to in vivo fatigue microdamage, J. Biomech. 18 (1985) 189–200, https://doi.org/10.1016/0021-9290(85)90204-0.
[20] V. Bentolila, T.M. Boyce, D.P. Fyhrie, R. Drumb, T.M. Skerry, M.B. Schaffler, Intracortical remodeling in adult rat long bones after fatigue loading, Bone 23 (1998) 275–281, https://doi.org/10.1016/S8756-3282(98)00104-5.
[21] Y. Bala, D. Farlay, P.D. Delmas, P.J. Meunier, G. Boivin, Time sequence of secondary mineralization and microhardness in cortical and cancellous bone from ewes, Bone 46 (2010) 1204–1212, https://doi.org/10.1016/j.bone.2009.11.032.
[22] G. Boivin, D. Farlay, Y. Bala, A. Doublier, P.J. Meunier, P.D. Delmas, Influence of remodeling on the mineralization of bone tissue, Osteoporos. Int. 20 (2009) 1023–1026, https://doi.org/10.1007/s00198-009-0861-x.
[23] G. Boivin, P.J. Meunier, Changes in bone remodeling rate influence the degree of mineralization of bone, Connect. Tissue Res. 43 (2002) 535–537, https://doi.org/10.1080/03008200290000934.
[24] P. Milovanovic, A. vom Scheidt, K. Mletzko, G. Sarau, K. Püschel, M. Djuric, M. Amling, S. Christiansen, B. Busse, Bone tissue aging affects mineralization of cement lines, Bone 110 (2018) 187–193, https://doi.org/10.1016/j.bone.2018.02.004.
[25] M. Langer, A. Pacureanu, H. Suhonen, Q. Grimal, P. Cloetens, F. Peyrin, X-ray phase

nanotomography resolves the 3D human bone ultrastructure, PLoS One 7 (2012) e35691, , https://doi.org/10.1371/journal.pone.0035691.
[26] M.T.K. Mulari, Q. Qu, P.L. Härkönen, H.K. Väänänen, Osteoblast-like cells complete osteoclastic bone resorption and form new mineralized bone matrix in vitro, Calcif. Tissue Int. 75 (2004) 253–261, https://doi.org/10.1007/s00223-004-0172-3.
[27] M.B. Schaffler, D.B. Burr, R.G. Frederickson, Morphology of the osteonal cement line in human-bone, Anat. Rec. 217 (1987) 223–228.
[28] K. Raum, I. Leguerney, F. Chandelier, M. Talmant, A. Säed, F. Peyrin, P. Laugier, Site-matched assessment of structural and tissue properties of cortical bone using scanning acoustic microscopy and synchrotron radiation μcT, Phys. Med. Biol. 51 (2006) 733–746, https://doi.org/10.1088/0031-9155/51/3/017.
[29] A. Ardizzoni, Osteocyte lacunar size-lamellar thickness relationships in human secondary osteons, Bone 28 (2001) 215–219, https://doi.org/10.1016/S8756-3282(00)00417-8.
[30] K.M. Hannah, C.D.L. Thomas, J.G. Clement, F. De Carlo, A.G. Peele, Bimodal distribution of osteocyte lacunar size in the human femoral cortex as revealed by micro-CT, Bone 47 (2010) 866–871, https://doi.org/10.1016/j.bone.2010.07.025.
[31] J. Power, M. Doube, R.L. van Bezooijen, N. Loveridge, J. Reeve, Osteocyte recruitment declines as the osteon fills in: interacting effects of osteocytic sclerostin and previous hip fracture on the size of cortical canals in the femoral neck, Bone 50 (2012) 1107–1114, https://doi.org/10.1016/j.bone.2012.01.016.
[32] P. Varga, A. Pacureanu, M. Langer, H. Suhonen, B. Hesse, Q. Grimal, P. Cloetens, K. Raum, F. Peyrin, Investigation of the three-dimensional orientation of mineralized collagen fibrils in human lamellar bone using synchrotron X-ray phase nanotomography, Acta Biomater. 9 (2013) 8118–8127, https://doi.org/10.1016/j.actbio.2013.05.015.
[33] S. Schrof, P. Varga, L. Galvis, K. Raum, A. Masic, 3D Raman mapping of the collagen fibril orientation in human osteonal lamellae, J. Struct. Biol. 187 (2014) 266–275, https://doi.org/10.1016/j.jsb.2014.07.001.
[34] W. Wagermaier, H.S. Gupta, A. Gourrier, M. Burghammer, P. Roschger, P. Fratzl, Spiral twisting of fiber orientation inside bone lamellae, Biointerphases. 1 (2006) 1–5, https://doi.org/10.1116/1.2178386.
[35] A. Faingold, S.R. Cohen, N. Reznikov, H.D. Wagner, Osteonal lamellae elementary units: Lamellar microstructure, curvature and mechanical properties, Acta Biomater. 9 (2013) 5956–5962, https://doi.org/10.1016/j.actbio.2012.11.032.
[36] H.S. Gupta, U. Stachewicz, W. Wagermaier, P. Roschger, H.D. Wagner, P. Fratzl, Mechanical modulation at the lamellar level in osteonal bone, J. Mater. Res. 21 (2006) 1913–1921, https://doi.org/10.1557/jmr.2006.0234.
[37] C. Ortiz, M. Dao, P. Vena, R. Contro, D. Carnelli, Orientation and size-dependent mechanical modulation within individual secondary osteons in cortical bone tissue, J. R. Soc. Interface 10 (2013) 20120953, https://doi.org/10.1098/rsif.2012.0953.
[38] J. Jowsey, M. Owen, J. Vaughan, Microradiographs and autoradiographs of cortical bone from monkeys injected with 90Sr, Br. J. Exp. Pathol. 34 (1953) 661–667 http://www.ncbi.nlm.nih.gov/pubmed/13115599.
[39] J. Jowsey, Studies of Haversian systems in man and some animals, J. Anat. 100 (1966) 857–864, https://doi.org/10.1002/ajpa.
[40] G. Boivin, P.J. Meunier, The degree of mineralization of bone tissue measured by computerized quantitative contact microradiography, Calcif. Tissue Int. 70 (2002) 503–511, https://doi.org/10.1007/s00223-001-2048-0.
[41] Y.N. Yeni, T.L. Norman, Fracture toughness of human femoral neck: effect of microstructure, composition, and age, Bone 26 (2000) 499–504, https://doi.org/10.1016/S8756-3282(00)00258-1.
[42] J.G. Skedros, C.J. Kiser, K.E. Keenan, S.C. Thomas, Analysis of osteon morphotype scoring schemes for interpreting load history: evaluation in the chimpanzee femur, J. Anat. 218 (2011) 480–499, https://doi.org/10.1111/j.1469-7580.2011.01348.x.
[43] R. Gauthier, M. Langer, H. Follet, C. Olivier, P.-J. Gouttenoire, L. Helfen, F. Rongiéras, D. Mitton, F. Peyrin, 3D micro structural analysis of human cortical bone in paired femoral diaphysis, femoral neck and radial diaphysis, J. Struct. Biol. 204 (2018) 182–190, https://doi.org/10.1016/j.jsb.2018.08.006.
[44] V. Bousson, F. Peyrin, C. Bergot, M. Hausard, A. Sautet, J.-D. Laredo, Cortical bone in the human femoral neck: three-dimensional appearance and porosity using synchrotron radiation, J. Bone Miner. Res. 19 (2004) 794–801, https://doi.org/10.1359/JBMR.040124.
[45] Z. Peter, V. Bousson, C. Bergot, F. Peyrin, A constrained region growing approach based on watershed for the segmentation of low contrast structures in bone micro-CT images, Pattern Recogn. 41 (2008) 2358–2368, https://doi.org/10.1016/j.patcog.2007.12.011.
[46] D.M.L. Cooper, B. Erickson, A.G. Peele, K. Hannah, C.D.L. Thomas, J.G. Clement, Visualization of 3D osteon morphology by synchrotron radiation micro-CT, J. Anat. 219 (2011) 481–489, https://doi.org/10.1111/j.1469-7580.2011.01398.x.
[47] Q. Vallet, N. Bochud, C. Chappard, P. Laugier, J.-G. Minonzio, In vivo characterization of cortical bone using guided waves measured by axial transmission, IEEE Trans. Ultrason. Ferroelectr. Freq. Control 63 (2016) 1361–1371, https://doi.org/10.1109/TUFFC.2016.2587079.
[48] B. Burt-Pichat, H. Follet, G. Toulemonde, M. Arlot, P. Delmas, R. Chapurlat, Methodological approach for the detection of both microdamage and fluorochrome labels in ewe bone and human trabecular bone, J. Bone Miner. Metab. 29 (2011) 756–764, https://doi.org/10.1007/s00774-011-0291-7.
[49] D. Paganin, S.C. Mayo, T.E. Gureyev, P.R. Miller, S.W. Wilkins, Simultaneous phase and amplitude extraction from a single defocused image of a homogeneous object, J. Microsc. 206 (2002) 33–40, https://doi.org/10.1046/j.1365-2818.2002.01010.x.
[50] I.S. Maggiano, C.M. Maggiano, J.G. Clement, C.D.L. Thomas, Y. Carter, D.M.L. Cooper, Three-dimensional reconstruction of Haversian systems in human cortical bone using synchrotron radiation-based micro-CT: morphology and quantification of branching and transverse connections across age, J. Anat. 228 (2016) 719–732, https://doi.org/10.1111/joa.12430.
[51] K. Schladitz, J. Ohser, W. Nagel, Measuring intrinsic volumes in digital 3d images, Discret. Geom. Comput. Imag. 4245 (2006) 247–258, https://doi.org/10.1007/11907350_21.
[52] D.W. Dempster, J.E. Compston, M.K. Drezner, F.H. Glorieux, J.A. Kanis, H. Malluche, P.J. Meunier, S.M. Ott, R.R. Recker, A.M. Parfitt, Standardized nomenclature, symbols, and units for bone histomorphometry: a 2012 update of the report of the ASBMR histomorphometry nomenclature committee, J. Bone Miner. Res. 28 (2013) 2–17, https://doi.org/10.1002/jbmr.1805.
[53] M.A. Parfitt, M.K. Drezner, F.H. Glorieux, J. a Kanis, H. Malluche, P.J. Meunier, S.M. Ott, R.R. Recker, Bone Histomorphometry : Standardization of Nomenclature, Symbols, and Units, vol. 2, (1987), pp. 595–610.
[54] E. Martín-Badosa, A. Elmoutaouakkil, S. Nuzzo, D. Amblard, L. Vico, F. Peyrin, A method for the automatic characterization of bone architecture in 3D mice microtomographic images, Comput. Med. Imaging Graph. 27 (2003) 447–458, https://doi.org/10.1016/S0895-6111(03)00031-4.
[55] J.G. Skedros, J.L. Holmes, E.G. Vajda, R.D. Bloebaum, Cement lines of secondary osteons in human bone are not mineral-deficient: new data in a historical perspective, Anat. Rec. A: Discov. Mol. Cell. Evol. Biol. 286 (2005) 781–803, https://doi.org/10.1002/ar.a.20214.
[56] A.G. Robling, S.D. Stout, Morphology of the drifting osteon, Cells Tissues Organs 164 (1999) 192–204, https://doi.org/10.1159/000016659.
[57] P. Atkinson, A. Hallsworth, The spatial structure of bone, in: R. Harrison, V. Navaratnam (Eds.), Prog. Anat, Cambridge University Press, Cambridge, 1982, pp. 179–199.
[58] G. Marotti, M.A. Muglia, C. Palumbo, Collagen texture and osteocyte distribution in lamellar bone, Ital. J. Anat. Embryol. (100 Suppl) (1995) 95–102.
[59] L.F. Bonewald, The amazing osteocyte, J. Bone Miner. Res. 26 (2011) 229–238, https://doi.org/10.1002/jbmr.320.
[60] T.A. Franz-Odendaal, B.K. Hall, P.E. Witten, Buried alive: how osteoblasts become osteocytes, Dev. Dyn. 235 (2006) 176–190, https://doi.org/10.1002/dvdy.20603.
[61] P.R. Buenzli, P. Pivonka, D.W. Smith, Bone refilling in cortical basic multicellular units: insights into tetracycline double labelling from a computational model, Biomech. Model. Mechanobiol. 13 (2014) 185–203, https://doi.org/10.1007/s10237-013-0495-y.
[62] P.R. Buenzli, Osteocytes as a record of bone formation dynamics: a mathematical model of osteocyte generation in bone matrix, J. Theor. Biol. 364 (2015) 418–427, https://doi.org/10.1016/j.jtbi.2014.09.028.
[63] G. Marotti, A.Z. Zallone, M. Ledda, Number, size and arrangement of osteoblasts in osteons at different stages of formation, Calcif. Tissue Res. 21 (1975) 96–101, https://doi.org/10.1007/BF02546434.
[64] M.A. Alias, P.R. Buenzli, Osteoblasts infill irregular pores under curvature and porosity controls: a hypothesis-testing analysis of cell behaviours, Biomech. Model. Mechanobiol. 17 (2018) 1357–1371, https://doi.org/10.1007/s10237-018-1031-x.
[65] M. McKee, A. Nanci, Osteopontin and the bone remodeling sequence, Ann. N. Y. Acad. Sci. 760 (1995) 177–189, https://doi.org/10.1111/j.1749-6632.1995.tb44629.x.
[66] F. Repp, P. Kollmannsberger, A. Roschger, M. Kerschnitzki, A. Berzlanovich, G. Gruber, P. Roschger, W. Wagermaier, R. Weinkamer, Spatial heterogeneity in the canalicular density of the osteocyte network in human osteons, Bone Rep. 6 (2017) 101–108, https://doi.org/10.1016/j.bonr.2017.03.001.
[67] B. Hesse, P. Varga, M. Langer, A. Pacureanu, S. Schrof, N. Männicke, H. Suhonen, P. Maurer, P. Cloetens, F. Peyrin, K. Raum, Canalicular network morphology is the major determinant of the spatial distribution of mass density in human bone tissue: evidence by means of synchrotron radiation phase-contrast nano-CT, J. Bone Miner. Res. 30 (2015) 346–356, https://doi.org/10.1002/jbmr.2324.
[68] K. Hoshi, S. Kawamoto, S. Ejiri, H. Ozawa, K. Tazawa, M. Tanaka, Osteocytic osteolysis observed in rats to which parathyroid hormone was continuously administered, J. Bone Miner. Metab. 22 (2004) 524–529, https://doi.org/10.1007/s00774-004-0519-x.
[69] M. Prideaux, C. Schutz, A.R. Wijenayaka, D.M. Findlay, D.G. Campbell, L.B. Solomon, G.J. Atkins, Isolation of osteocytes from human trabecular bone, Bone 88 (2016) 64–72, https://doi.org/10.1016/j.bone.2016.04.017.
[70] R.T. Ormsby, L.B. Solomon, D.M. Findlay, G.J. Atkins, M. Cantley, D.R. Haynes, M. Kogawa, Evidence that osteocyte perilacunar remodelling contributes to polyethylene wear particle induced osteolysis, Acta Biomater. 33 (2016) 242–251, https://doi.org/10.1016/j.actbio.2016.01.016.
[71] H. Qing, L.F. Bonewald, Osteocyte remodeling of the perilacunar and pericanalicular matrix, Int. J. Oral Sci. 1 (2009) 59–65, https://doi.org/10.4248/ijos.09019.
[72] A. Roschger, P. Roschger, W. Wagermaier, J. Chen, A. van Tol, F. Repp, S. Blouin, A. Berzlanovich, G.M. Gruber, K. Klaushofer, P. Fratzl, R. Weinkamer, The contribution of the pericanalicular matrix to mineral content in human osteonal bone, Bone (2019), https://doi.org/10.1016/j.bone.2019.03.018 #pagerange#.
[73] E.A. Zimmermann, C. Riedel, F. Schmidt, K. Stockhausen, Y. Chushkin, E. Schaible, B. Gludovatz, E. Vettorazzi, F. Zontone, K. Püschel, M. Amling, R. Ritchie, B. Busse, Mechanical competence and bone quality develop during skeletal growth, J. Bone Miner. Res. (2019) 0–3, https://doi.org/10.1002/jbmr.3730.
[74] M.B. Schaffler, K. Choi, C. Milgrom, Aging and matrix microdamage accumulation in human compact bone, Bone 17 (1995) 521–525, https://doi.org/10.1016/8756-3282(95)00370-3.
[75] F.J. O'Brien, D. Taylor, T.C. Lee, The Effect of Bone Microstructure on the Initiation and Growth of Microcracks, (2005), https://doi.org/10.1016/j.orthres.2004.08.005.
[76] N.J. Wachter, P. Augat, G.D. Krischak, M. Mentzel, L. Kinzl, L. Claes, Prediction of cortical bone porosity in vitro by microcomputed tomography, Calcif. Tissue Int. 68 (2001) 38–42, https://doi.org/10.1007/s002230001182.
[77] A.A. Griffith, The phenomena of rupture and flow in solids, Philos. Trans. R. Soc. A

Math. Phys. Eng. Sci. 221 (1921) 163–198, https://doi.org/10.1098/rsta.1921.0006.

[78] V. Canè, G. Marotti, G. Volpi, D. Zaffe, S. Palazzini, F. Remaggi, M.A. Muglia, Size and density of osteocyte lacunae in different regions of long bones, Calcif. Tissue Int. 34 (1982) 558–563, https://doi.org/10.1007/BF02411304.

[79] H. Chen, X. Zhou, S. Shoumura, S. Emura, Y. Bunai, Age- and gender-dependent changes in three-dimensional microstructure of cortical and trabecular bone at the human femoral neck, Osteoporos. Int. 21 (2010) 627–636, https://doi.org/10.1007/s00198-009-0993-z.

[80] A.J. Burghardt, G.J. Kazakia, S. Ramachandran, T.M. Link, S. Majumdar, Age- and gender-related differences in the geometric properties and biomechanical significance of intracortical porosity in the distal radius and tibia, J. Bone Miner. Res. 25 (2010) 983–993, https://doi.org/10.1359/jbmr.091104.

[81] B. Busse, D. Djonic, P. Milovanovic, M. Hahn, K. Püschel, R.O. Ritchie, M. Djuric, M. Amling, Decrease in the osteocyte lacunar density accompanied by hypermineralized lacunar occlusion reveals failure and delay of remodeling in aged human bone, Aging Cell 9 (2010) 1065–1075, https://doi.org/10.1111/j.1474-9726.2010.00633.x.